

Low-Field MRI: An MR Physics Perspective

José P. Marques,^{1*} Frank F.J. Simonis,² and Andrew G. Webb, PhD³

Historically, clinical MRI started with main magnetic field strengths in the $\sim 0.05\text{--}0.35\text{T}$ range. In the past 40 years there have been considerable developments in MRI hardware, with one of the primary ones being the trend to higher magnetic fields. While resulting in large improvements in data quality and diagnostic value, such developments have meant that conventional systems at 1.5 and 3T remain relatively expensive pieces of medical imaging equipment, and are out of the financial reach for much of the world. In this review we describe the current state-of-the-art of low-field systems (defined as 0.25–1T), both with respect to its low cost, low foot-print, and subject accessibility. Furthermore, we discuss how low field could potentially benefit from many of the developments that have occurred in higher-field MRI.

In the first section, the signal-to-noise ratio (SNR) dependence on the static magnetic field and its impact on the achievable contrast, resolution, and acquisition times are discussed from a theoretical perspective. In the second section, developments in hardware (eg, magnet, gradient, and RF coils) used both in experimental low-field scanners and also those that are currently in the market are reviewed. In the final section the potential roles of new acquisition readouts, motion tracking, and image reconstruction strategies, currently being developed primarily at higher fields, are presented.

Level of Evidence: 5

Technical Efficacy Stage: 1

J. MAGN. RESON. IMAGING 2019;49:1528–1542.

Over the last three decades there has been a remarkable increase in the availability of magnetic resonance imaging (MRI) in developed countries, with it increasingly being used as a diagnostic tool that has a therapeutic impact. Many radiology departments even in small hospitals and clinics now have access to this technology. From an MR hardware point of view there have been quite dramatic improvements in the sophistication and performance of each component of the system: field strengths have increased but the magnet footprint has decreased, gradient strengths/slew rates and stability have increased, and the number of receive channels is now standardly 16 or 32, with 64 on the horizon. 1.5T has become the standard clinical machine even in very small hospitals, almost completely replacing the older lower field strength (0.2–1T) machines that had an important role in the development of MRI during the 1980s. There are now approximately the same number of 1.5T and 3T systems being ordered worldwide.¹ Over the last decade, there has also been an increase in the number of whole-body 7T systems, many of which have been developed to the stage of performing

targeted clinical and clinical research studies. These general improvements have also led to various improvements in data acquisition and image reconstruction strategies, such as compressed sensing,² fingerprinting,³ and the use of artificial intelligence.^{4,5}

However, the increase in access to sophisticated MRI systems is extremely inhomogeneous worldwide, with MRI scarcely, if at all, available in underdeveloped and developing countries. Worldwide only one-tenth of the population has access to MRI, and even within developed countries an inhomogeneous distribution of this important diagnostic tool persists.^{6,7} The highest number (~ 50) of available scanners per million inhabitants is found in Japan, which coincidentally has a policy that has facilitated the spread and availability of low-field scanners,⁸ while in India and China the number of available scanners is much lower (~ 0.89). There are two main factors responsible for this: 1) the price of installation the systems and postinstallation maintenance, and 2) the complexity of operating an MR system. The superconducting magnet represents a significant portion of the overall cost, with very

View this article online at wileyonlinelibrary.com. DOI: 10.1002/jmri.26637

Received Sep 20, 2018, Accepted for publication Nov 28, 2018.

*Address reprint requests to: J.P.M., Donders Centre for Cognitive Neuroimaging Kapittelweg 29 6525 EN Nijmegen, The Netherlands.
E-mail: j.marques@donders.ru.nl

From the ¹Radboud University, Donders Institute for Brain, Cognition and Behaviour, Nijmegen, The Netherlands; ²Magnetic Detection & Imaging, Technical Medical Centre, University of Twente, The Netherlands; and ³C.J.Gorter Center for High Field MRI, Department of Radiology, Leiden University Medical Centre, The Netherlands

This is an open access article under the terms of the Creative Commons Attribution-NonCommercial License, which permits use, distribution and reproduction in any medium, provided the original work is properly cited and is not used for commercial purposes.

high requirements on the homogeneity and temporal stability. On older systems, there are significant costs for helium refills and the upkeep of the cryostats mechanical refrigerators/cold heads. The improvements in scanner hardware and technology, briefly referred to in the previous paragraph, have also resulted in systems becoming more expensive, counteracting the normal economic model in which technology drops in price over time.

Given the extraordinary imbalance in healthcare availability in the developed and developing worlds, there is increasing interest in the MRI community in revisiting the approach of using low-field MRI, which, while not producing the highest-quality images, nevertheless should be able to provide diagnostically useful information. Advances in permanent magnet design, RF coil architecture, gradient performance, and image processing algorithms developed for conventional MRI systems can also be applicable to lower field strengths. Lower-power RF and gradient amplifiers should suffice, as the target spatial resolutions will be lower. The reduction in field strength also has benefits from a subject safety and comfort perspective, in terms of reduced projectile risks (scales with B_0 dB₀/dr), implant compliance, and the possibility to image closer to implants due to smaller magnetic susceptibility artifacts (scales with B_0), reduced specific absorption rate (SAR) limitations (scales with B_0^2), and reduced acoustic noise because of lowered forces on the gradient coil windings with a given current amplitude (scales with B_0). The other main attractive point of low-field systems is their reduced footprint, which could take MRI to the point-of-care, similar to ultrasound. In many cases the decreased image quality compared to high-field MRI systems does not translate into worsened patient outcome.

One example very relevant to the developing world is congenital and neonatal hydrocephalus, which is characterized by cerebrospinal fluid (CSF) accumulation in the ventricles and brain spaces accompanied by an increase in intracranial pressure. These have a relatively high incidence in the developing world compared to the developed world,⁹ but much higher in the developing world. Low-field MRI could have an important diagnostic value in the diagnosis of these pathologies. In this particular case, and ones that address specific diseases endemic to the developing world, low field has particular attractions. First and foremost is the reduced financial cost. Second is the potential to have a much more sustainable (relatively inexpensive repair and replacement of hardware modules) system than a superconducting magnet-based system. Third is the reduced siting requirements in terms of space/power/cooling. In addition, specific to neonatal applications are the vastly reduced acoustic noise, the open nature that allows direct parental participation, and the much lower SAR that have been addressed in the previous paragraph.

This review has the following structure. First, the effective signal-to-noise ratio (SNR) dependence on magnetic field strength of the various imaging contrasts (T_1 -weighted, T_2^* -weighted and PD) is analyzed and reviewed. The second

section reviews the current trends and developments in the various hardware components of an MRI scanner. The third section is devoted to current low-field systems present in the market, and their main clinical application focus. The fourth section covers signal acquisition strategies that are well established in other fields of research, and the impact they could have in low-field imaging, potentially significantly improving what can be achieved with respect to what was done in the early days of MRI.

Field Dependence of the SNR and Relaxation Times

SNR

The MRI signal is proportional to: 1) the induced nuclear magnetization, which increases linearly with B_0 , and 2) the rate of change of the magnetic flux, Faraday's law, representing the detected signal from the precession frequency of the magnetization, that also scales linearly with B_0 . Taken together, the MRI signal has a quadratic dependence on the static magnetic field. The noise has contributions from both the coil and the sample, each of which gives noise voltages expressed by the Johnson noise model¹⁰ in terms of its root mean square value(s):

$$\sigma_{V_{\text{noise}}} = \sqrt{4k_B BW (T_{\text{coil}} R_{\text{coil}} + T_{\text{sample}} R_{\text{sample}})}$$

where R_{coil} , T_{coil} , and R_{sample} , T_{sample} are the equivalent resistances and temperatures of the coil and sample, and BW is the bandwidth used in the signal acquisition. In the RF coil, alternating electrical currents flow on the outer surfaces of its conductors due to the skin effect, and the resistance is inversely proportional to the effective cross-section of the conductor, and thus proportional to $B_0^{1/2}$. On the sample side, at low frequencies it has been shown that resistance has a quadratic dependence on B_0 .¹⁰ In the range of fields addressed in this article (0.25–1T), the contributions from coil noise and sample noise could be approximately equal, and so a good assumption would be that the SNR scales with $B_0^{3/2}$.

Relaxation Parameters

In the range of fields discussed in this review, tissue longitudinal (T_1) relaxation times increase with magnetic field while (apparent) transverse (T_2^*) relaxation times decrease. There is a surprisingly small body of literature on the field dependence of these values for different tissues. One of the few studies over a large range of magnetic fields (0.2–7T) was performed by Rooney et al.,¹¹ which found that most soft brain tissues followed the phenomenological model proposed by Bottomley et al.¹² where $T_1(ms) = a(\gamma B_0)^b$, where γ is the gyromagnetic constant given in Hz/T. The parameters a and b were found to be 0.71/1.16/3.35 and 0.382/0.376/0.340 for white matter (WM), gray matter (GM), and blood, respectively. CSF, on the other hand, was found to have no discernible field dependence. Apparent transverse relaxation of various brain regions

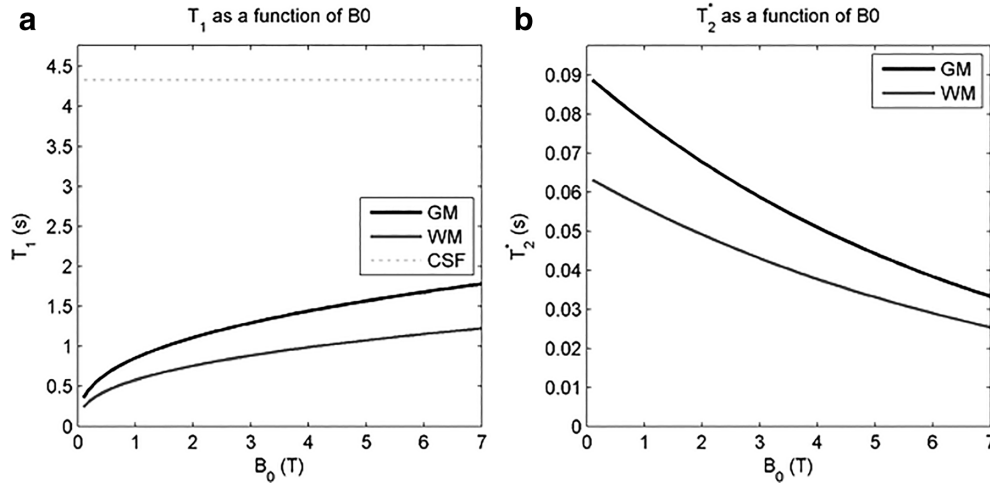


FIGURE 1: Plot of the dependence of relaxation times as a function of magnetic field using for the (a) longitudinal relaxation the fit measured by Rooney et al.¹¹ and (b) for the apparent transverse relaxation the fits obtained by Pohmann et al.¹⁴

have been reported on the same subjects from 1.5T to 7T by Peters et al.¹³ In that study, a linear model of the apparent transverse relaxation rate dependence on the static magnetic field was assumed ($R_2^* = a + bB_0$). While this is a well-established model for R_2' (it assumes the dephasing has its origin in susceptibility sources in the static dephasing regime), it fails at lower field strengths,¹³ as the relaxation times are no longer dominated by R_2' and approach R_2 (note that $R_2^* = R_2 + R_2'$). By pooling measurements from various studies, Pohmann et al.¹⁴ used a phenomenological model where $T_2^*(ms) = ae^{-bB_0}$, with a and b being 90/64 and 0.142/0.132 for gray and white matter, respectively. These two models (see Fig. 1) will be used throughout the article to discuss some of the expected behavior of contrast as a function of magnetic field.

Quantifying the Field Dependence of SNR and CNR Efficiencies of Different Contrast Weightings

For the purpose of further discussion, we define the $SNR_{eff,w}$ to reflect the SNR efficiency of a sequence with a given weighting, w, as being its SNR_w divided by the square root of the repetition time (TR) of the sequence. $TR^{\frac{1}{2}} \cdot SNR_w$ represents not only the SNR dependence on magnetic field, but also that resulting from optimum sequence parameters associated with the field-specific relaxation times. $SNR_{eff,w}$ will be assumed to be proportional to $B_0^{power_{eff,w}}$. Where $power_{eff,w}$ is the effective power law associated with a given image weighting taking into account the relaxation variation with magnetic field. In such a formalism, the SNR at a given isotropic spatial resolution (res), acquired in given period of times, T_{ACQ} , is given by $SNR_{eff,w} \cdot T_{ACQ}^{1/2} \cdot res^3$. Thus, to acquire an image at lower magnetic field, B_{0L} , with the same resolution as one at high magnetic field, B_{0H} , while maintaining the same SNR or contrast-to-noise ratio (CNR), an increased number of averages are needed, resulting in an increased acquisition time given by:

$$T_{ACQL} = \left(B_{0,H} / B_{0,L} \right)^{2 \cdot power_{eff,w}} T_{ACQH} \quad (1)$$

This results in a supra-linear increase of the acquisition time with respect to a decrease in magnetic field. If we consider as a reference the Alzheimer's Disease Neuroimaging Initiative (ADNI) brain protocol¹⁵ where 1.2 mm isotropic T_1 -weighted image datasets were acquired in 9 minutes, reducing the magnetic field from 1.5 to 0.5T would suggest an increase of the acquisition time to 91 or 243 minutes in the case of a linear or 3/2 effective power dependence of the SNR, respectively. Obviously, the spatial resolution has to be sacrificed, and given the relationship:

$$res_L = \left(B_{0,H} / B_{0,L} \right)^{power_{eff,w}/3} res_H \quad (2)$$

the 1.2 mm isotropic protocol would have to be adapted to a 1.7 mm isotropic resolution to keep the acquisition time the same. The number of phase encoding steps per acquisition is given by:

$$PE_L = \left(B_{0,L} / B_{0,H} \right)^{2/3 \cdot power_{eff,w}} PE_H \quad (3)$$

In the case of the example above (moving from 1.5 to 0.5T), it would imply that only half of the phase encoding steps would be needed, and the SNR could then be matched by acquiring the image with two signal averages. An advantage of this is that the sensitivity to scanner drifts and subject motion is reduced. In practice a compromise between these two approaches (increase of total scan time and reduction of the spatial resolution) would generally be sought when moving to lower fields.

Another important aspect when considering the effective cost of moving to lower fields is the value of $power_{eff,w}$. To evaluate this we considered three different contrasts: proton

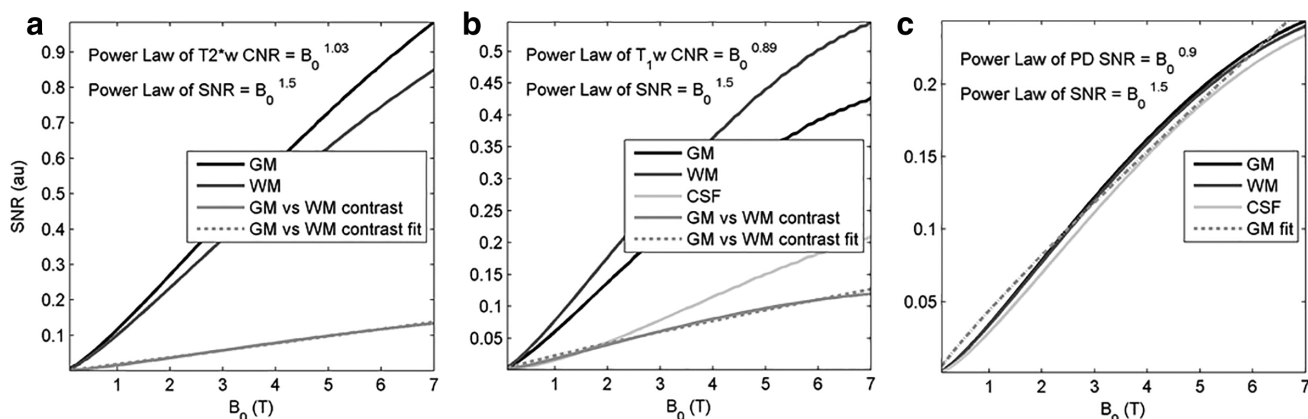


FIGURE 2: Plots of (a) T_2^* , (b) T_1 -weighted, and (c) PD SNR for an optimized protocols at each given field strength. Dashed lines correspond to the fit of the relevant contrast with a function $c B_0^{\text{power}_{\text{eff},w}}$, where b is the power law reported in each plot.

density (PD), T_1 -weighted (T_{1w}), and T_2^* -weighted contrast ($T_{2,w}^*$). For this analysis we used the CNR obtained between gray and white matter, as these are the only values that are available from the literature over a large range of field strengths. As mentioned above, the SNR is assumed to be proportional to $B_0^{3/2}$. For the sake of simplicity, we assumed that each of these acquisitions would be performed using a gradient recalled echo whose SNR is given by:

$$SNR_{\text{issue}} = B_0^{\frac{3}{2}} \frac{1}{\sqrt{BW}} \sin(\alpha_w) e^{-\frac{TE}{T_{2,tissue}^*}} \frac{1 - e^{-TR/T_{1,tissue}}}{1 - \cos(\alpha) e^{-TR/T_{1,tissue}}} \quad (4)$$

where the flip angle (α), repetition time (TR), echo time (TE) and bandwidth (BW) were optimized for each specific field strength and contrast. For T_{1w} and PD contrast, TE was set to 1/8 of the $T_{2,WM}^*$ of white matter at the given field strength, while in $T_{2,w}^*$ imaging it was set to optimize the contrast between WM and GM. The BW was always chosen to optimize SNR, ie, the readout duration was always set to 2TE minus a given dead time, while the TR was set to 2TE. The dead time was set to 3 msec, assumed to be field-independent, and corresponds to the time needed to apply an excitation RF pulse and any gradient pre-phasers or crushers. The flip angle for PD and $T_{2,w}^*$ contrast were set to 1/4 of the Ernst angle and the Ernst angle, respectively, while for T_{1w} contrast it was computed to maximize the contrast between gray and white matter. Figure 2 shows the computed field dependence of these three contrasts. It is interesting to note that for all three MR contrast types, the power law observed is lower than that initially postulated (1.04, 0.90, and 0.92 for the T_2^* , T_{1w} , and PD contrasts, respectively). MatLab (MathWorks, Natick, MA) code is provided in a github released repository using zenodo, <http://doi.org/10.5281/zenodo.1629523>. Thus, the SNR loss from moving to a lower magnetic field is, in the case of brain imaging, smaller than what would be predicted. The implication of this information of this observation is that in the

above discussion on resolution, acquisition time and phase encoding steps the least penalizing option can be used throughout.

Advances in Hardware

The earliest human MR images were obtained at magnetic fields between 0.05 and 0.35T using various forms of electromagnets and/or permanent magnets. Magnet homogeneity and stability were relatively poor, with gradients powered by reconfigured audio amplifiers, and used simple single coil RF transmitters and receivers. One famous system developed in Paul Lauterbur's laboratory, shown in Fig. 3, was described by Simon¹⁶ as:

“The magnet is a four coil air-core design operating at 939 gauss (93.9 mT). The direction of the magnetic field is perpendicular to the planes of the coils. The bore diameter of the outer coils is 62 cm. The x and y gradient coils were constructed by winding #8 copper wire in a frame made of 1 inch aluminum channel. The higher order terms were less than 1% over a 40 cm diameter in the center of the magnet. The coil for the z-gradient was constructed by winding #8 copper wire into two rings of 1 inch aluminium channel placed inside the magnet. The z-gradient is linear to within 1% over approximately 20 cm near the center of the magnet. The maximum amplitude is 420 Hz/cm, with a rise time of each gradient less than 10 msec.”

Since that time significant advances have been made in magnet, gradient, and RF design for low-field systems. This section describes the current state-of-the-art in both commercial and research low-field systems.

Magnet Geometries

Magnets should have homogeneities on the order of parts-per-million (ppm) over an ellipsoidal imaging volume, with fluctuations during the scan period of less than 100 nT (note that since low-field systems are typically used for body rather than head imaging, the field homogeneity is often

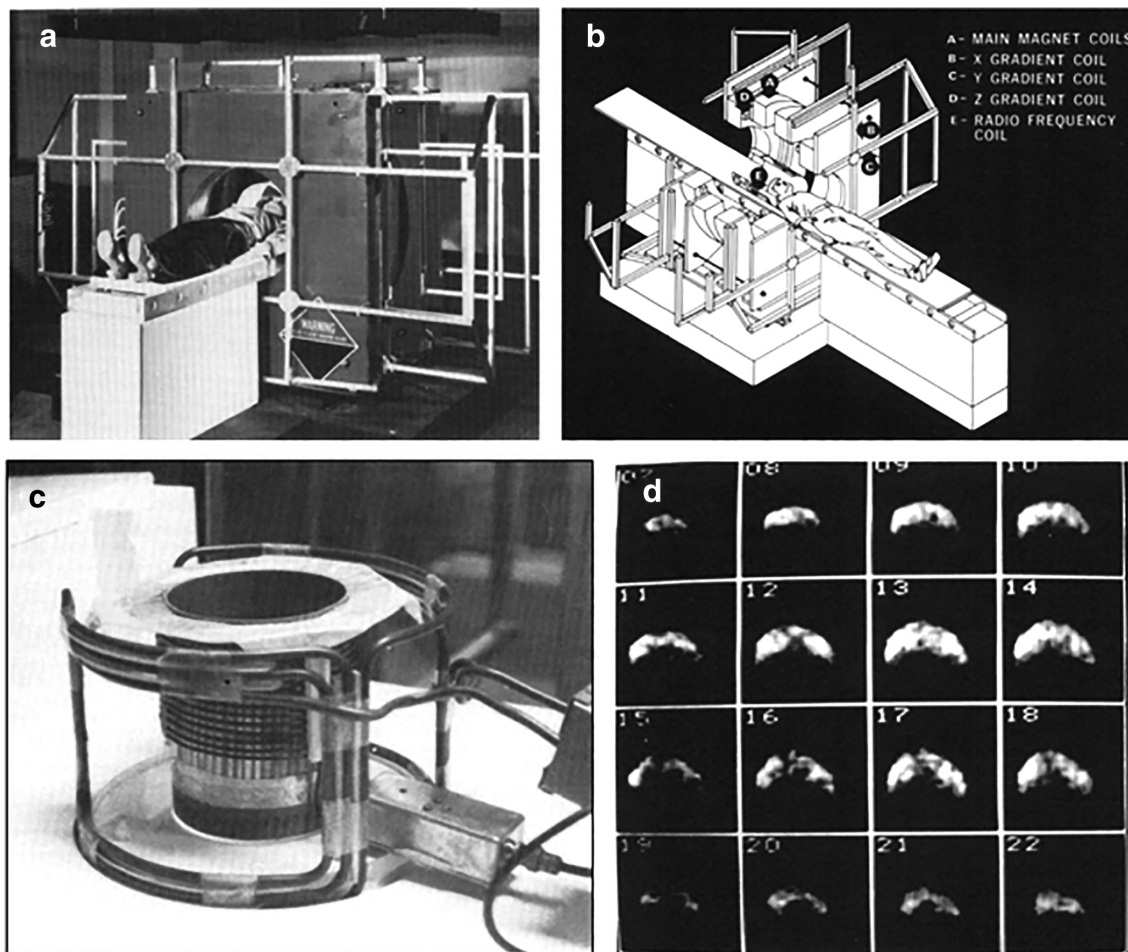


FIGURE 3: Historical photographs and sketches showing one of the first MRI systems to produce human images, together with the RF coil and in vivo breast images.

specified in terms of an ellipsoidal volume rather than a diameter-of-spherical-volume, which is standard for higher field clinical systems). For low-field systems operating at between 0.25 and 0.5T, there are two basic choices of magnet, one based purely on a permanent magnet based on neodymium-iron-boron,¹⁸⁻²⁰ or one that combines a permanent magnet with an additional electromagnet.¹⁷ For fields higher than 0.5T, superconductors are normally used.

There are two basic geometries of permanent magnet, the H-shaped one shown in Fig. 4a or the more common C-shaped one shown in Fig. 4b. The difference is either having a single ferromagnetic yoke (C-shaped) or two yokes (H-shaped) to transport the flux. Two large discs of permanent magnet material are placed above and below the gap in which the patient is positioned. These permanent magnet discs in fact consist of many different-sized much smaller pieces of materials, the geometries of which are optimized to produce the strongest and most homogeneous field. The magnetic field may be further shaped by using ferromagnetic pole pieces. In addition to the open access, one of the major advantages of such systems is the very low siting requirements due to the almost complete absence of fringe fields. For example, a commercial 1T hand/wrist imager can be sited in an

area of only 3 × 4 meters, albeit requiring a floor that can support almost 2000 kg (see Table 1).

Magnet Materials

One of the main advances in permanent magnet technology has been the increased availability of raw materials (in terms of rare earths mainly mined in China) and the development of methods for high-quality machining of such materials. As mentioned previously, the main material used for permanent magnets is Neodymium-iron-boron (NdFeB, Nd₂B₁₄Fe), which is available with remanences (B_r) ranging from ~1.2 to 1.425T. The remanence is defined as the magnetic flux density after a material has been magnetized; the higher the value, the stronger the magnetic field both within and surrounding the magnet. NdFeB is available in many grades, eg, N35, N42, N48, N50, and N52, where the number describes the maximum energy product in units of mega-Gauss-Oersteds (MGOe). N52 has the highest field strength, but when a higher coercivity (the reverse driving field required to demagnetize the magnet) is required, then a harder grade such as N48 M or N48H gives a larger safety margin with respect to potential demagnetization. The harder grades are mechanically not as strong and also more expensive

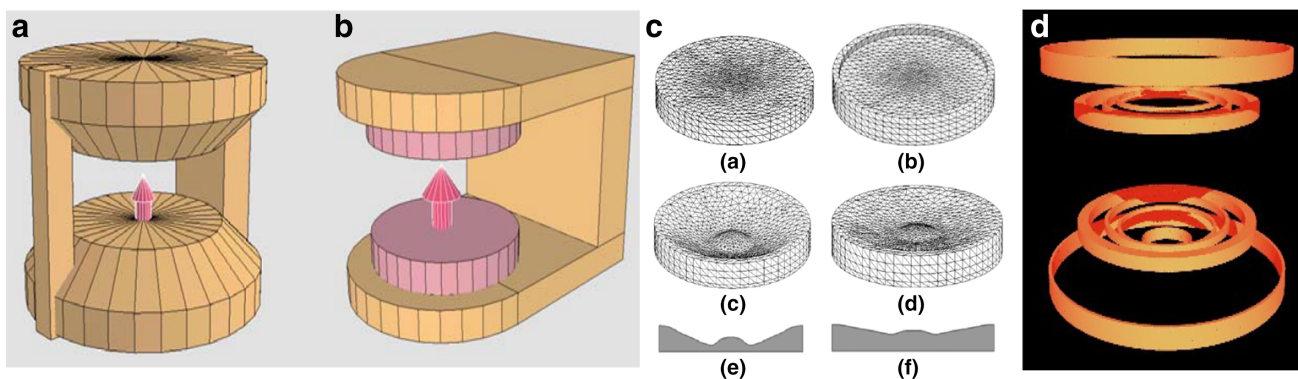


FIGURE 4: Schematics of different types of permanent low-field magnet. (a) An H-shaped system, with two ferromagnetic yokes and two permanent magnets with shaped ferromagnetic pole-pieces. (b) The most common C-shaped geometry with one ferromagnetic yoke. (c) Examples of steps to improve the magnetic field inhomogeneity by changing the shape of the pole pieces (adapted from Tadic et al²¹). (d) For higher magnetic fields electromagnets can be incorporated, as well as a shielding coil. These can be either regular conductors or superconductors for field of 1T and above.

due to the larger traces of rare earth elements such as dysprosium. In the manufacturing process the individual chemical elements are melted in a vacuum-induction furnace to form an alloy, cooled, and then ground into particles a few micrometers in size. This powder is pressed into the appropriate mold and then a strong magnetic field applied. The material is then demagnetized and sintered in an oxygen-free environment. Rapid cooling is followed by machining into the appropriate shape and size. The material is cleaned and a nickel-copper-nickel coating applied. Finally, the magnet is remagnetized.

The magnetic field produced by a permanent magnet can be calculated via the vector potential (A) at point x :

$$\vec{A}(\vec{x}) = \frac{\mu_0}{4\pi} \oint \frac{\vec{M}(\vec{x}') \times \vec{n}'}{|\vec{x} - \vec{x}'|} da' \quad (5)$$

where M is the volume magnetization of the magnet, n is the unit vector normal to the surface at point x' and μ_0 is the permeability of vacuum. The integral is evaluated over the entire surface (a) of the magnet. For a cylindrical permanent magnet with radius R and thickness T , the field on the z -axis is given by:

$$B(z) = \frac{\mu_0 M}{2} \left(\frac{z}{\sqrt{z^2 + R^2}} - \frac{z - T}{\sqrt{(z - T)^2 + R^2}} \right) \quad (6)$$

In practice, the homogeneity of the magnetic field from a purely cylindrical geometry can be improved by shaping the permanent magnet,²¹ as shown in Fig. 4. After the field has been measured, it can be further improved by analyzing the remaining field inhomogeneities in terms of spherical harmonics or other basis functions, and then optimized by adding small moveable magnetic pieces.^{22,23} Electrical shim coils

can also be used as an alternative method to optimize the field homogeneity.²⁴

In terms of research magnets, McGinley et al²⁵ have recently proposed a new permanent magnet design that produces a main magnetic field parallel (as opposed to the conventional perpendicular) to the pole pieces, which potentially allows rotation of the magnet with respect to the object. In this way, it is possible to obtain images with the so-called magic angle between the direction of the static magnetic field and the orientation of the structures of interest. This arrangement increases the effective T_2 time in structures such as ligaments and cartilage in which dipolar coupling is dominant.

Gradient Design

The gradients used in the original low-field magnets in the 1980s typically had strengths of a few hundred Hz/cm with rise times of a few milliseconds, and were driven by modified audio amplifiers. Significant improvements have been made over the past decades in terms of producing gradient assemblies with high efficiency and linearity with short switching times. The geometry of the gradients is different from those used in clinical 1.5 and 3T cylindrical bore magnets. Usually an open MRI system uses a pair of planar coils (see Fig. 5), referred to as bi-planar gradient coils,²⁶ which are attached to the two opposing magnetic poles: this configuration maximizes the open space in the magnet gap. There have been many publications outlining advances in the design of such bi-planar gradients.^{27–29}

In terms of gradient performance, typical numbers for modern-day gradients on the “whole body” low-field MRI systems are inductances on the order of 300–500 μH , resistances of 3–4 Ω , and efficiencies of 4–8 mT/m/A. Maximum gradient strengths for water-cooled gradient coils are on the order of 25 mT/m with a slew rate of 50 T/m/s. For comparison, a state-of-the-art 1.5 or 3T system has maximum gradients of 45 mT/m with a slew rate of 200 T/m/s. In the case

TABLE 1. Overview of low field MRI system specifications currently commercially available. Specifications were obtained from the various manufacturers websites and owner manuals.

Vendor	Esate-Gscan Brio	Esate O scan	Paramed-OpenMR	Fonar-Upleft	AspectImaging-Embrace	Aspect Imaging-Wristview	Bazda-Polar 35	Bazda-Polar 50	Neusoft-Superstar 0.35T	ViewRay-MRIdian	Medonica-MagVue 0.33T	Revték-GB-0.5T	Anke-Openmark 5000, 4000 and III	Wandong-i_Open
Field (T)	0.25	0.31	0.5	0.6	1	1	0.35	0.5	0.35	0.35	0.33	0.5	0.51, 0.4, 0.3	0.5,0.4, 0.36,0.3T
Type: permanent (p), superconducting (s), s cryogen free (scf)	p	p	scf	r	p	p	p	p	p	s	p	p	p	p
Weight (tons)	10		22.7	111	5.5	1.05	17.5	27	19.5			22		
Space (m2)	23	9	22	21	22.3	12	25	30	30		30			
5 Gauss line from center (m)	1.8			not always on and not shielded	within cover	0.6					1.75			
Gradient (mT/m, mT/m/ms)	20, 56	20,51	20, 33,3	20, 33	150, 454	215, 1074 (limited to 650 due to PNS)	18,60	25,75	26,67	18,200	20,40			
Imaging diameter sphere (cm)	27	14	30		12x13x13	12x12x7	40	40	36	50	40			
Bore size (cm)	37.5 (35.1 incl bed)		58	46	18x26	7.6x20	40.5	40.5	38	70 (diameter)	42	41		
RF amplifier (kW)	2x 1.5	1.5	9				5	6	6		6			
Voltage (V)	220	220	400-480	400-480	220	220					220			

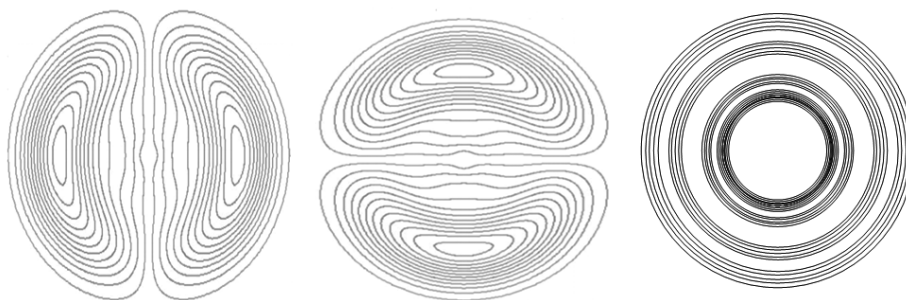


FIGURE 5: Wire patterns used to produce the (left and center) x- and y-gradients and (right) the z-gradient. The gradients form pairs with one of each set placed flat on the pole pieces of the magnet.

of a reduced bore magnet for hand/wrist scanning, with an active imaging volume of $120 \times 120 \times 70$ mm, the maximum gradient strength can reach up to 215 mT/m with a maximum slew rate of 1074 mT/m/s which, due to peripheral nerve stimulation (PNS) limits, can practically be operated up to 650 mT/m/s. Neonatal imaging systems with larger active imaging volumes of $130 \times 130 \times 120$ mm are available, with maximum gradient strengths of 150 mT/m and a rise time of 300 μ s.

Although the performance of bi-planar gradient coils is intrinsically lower than ones formed on a cylindrical surface, as outlined in the first section of this review, the spatial resolution of low-field images is lower than those acquired at higher fields, and so gradient performance is not a limiting factor to image acquisition. It should also be noted that one of the advantages of the lower fields is the reduced Lorentz forces, which typically result in a much reduced acoustic noise level, which is highly desirable for patient studies.³⁰

RF Coils

The vertical orientation of the B_0 field in most low-field systems means that a solenoid coil can be used. This geometry has an intrinsic 2–3-fold higher efficiency than a transverse resonators such as the birdcage coil that forms the “body coil” incorporated into the cylindrical bore of a 1.5 or 3T clinical system. Commercial systems also exist in which the patient can either stand or lie down: in these cases the solenoid coil can be placed around the head or thorax, with its main axis

of the solenoid coil aligned along the length of the body. Although systems generally use the solenoid as both the transmitter and receiver, solenoid coils can also be formed into individual array elements, as described by Su et al.³¹

One of the major advances in the past two decades in clinical systems has been the incorporation of multiple receive elements (receive arrays) both for higher SNR and also reduced imaging time using parallel imaging techniques. In terms of low-field MRI, at the lower end of 0.25T the noise is dominated by the contribution of losses in the RF coil, whereas at the higher end of 1T the noise contribution from the body starts to become significant. Many low-field systems now incorporate receive arrays,³² with these elements being of relatively large size so that coil noise does not dominate (examples are shown in Fig. 6). In this way there is an SNR gain mainly in the periphery of the image, and the use of multiple receive elements also enables faster scanning times through sparse sampling of k -space and image reconstruction,^{33,34} so-called parallel imaging. Commercial systems typically include up to four different coils, with a maximum of 13 elements offered by one vendor. Using the latter system, simultaneous high-resolution imaging of both breasts can be performed in both coronal and transverse directions. For many arrays the basic geometry consists of a combination of loops and butterfly coils, as illustrated in Fig. 6d for a four-element array designed for thorax imaging;³⁵ in this case, the dimensions of the array were optimized to minimize the geometry factor (g-factor) for parallel imaging with a SENSE factor of four.

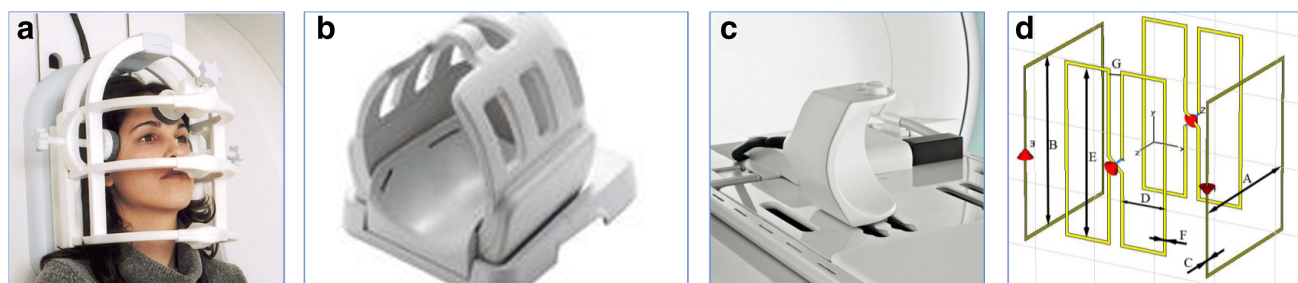


FIGURE 6: Examples of RF coils used on low-field MRI systems. (a) Quadrature transmit/receive coil on the vertical 0.6T Fonar system, (b) Four-element head array on the 0.25T Esaote. (c) Shoulder phased array for the Siemens 0.35T Magnetom. (d) One example of a research phased array designed for 0.25T with a loop/butterfly coil arrangement. (a–c courtesy of FONAR Corporation, Esaote and Siemens Healthineers, respectively).

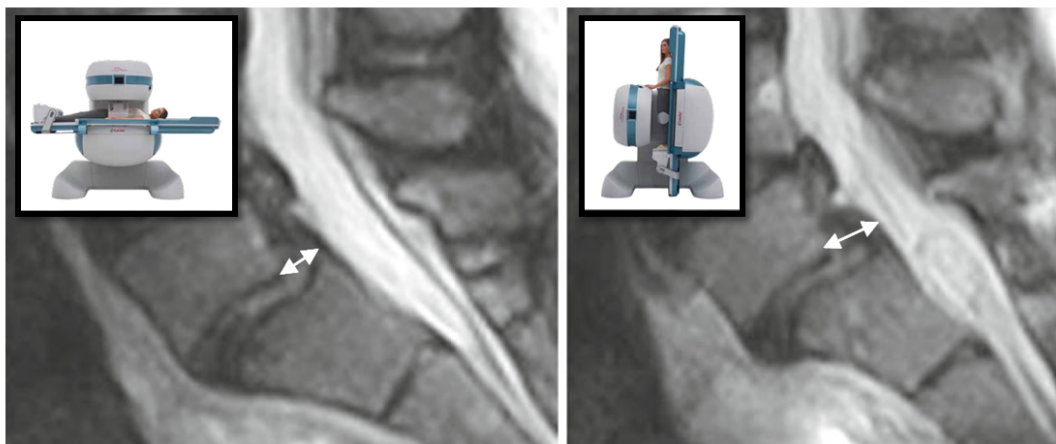


FIGURE 7: Fast spin-echo T₂-weighted scans in the sagittal plane of the lumbar spine acquired at 0.25T. The left image is made in the supine position and the right image in the upright position. In the right image the disc protrusion becomes more evident. Adapted from Tarantino et al.⁴⁵ Inserts within each figure demonstrate the functionality of the ESAOTE rotatable permanent magnet that could be used to acquire such images.

Overview of the Main Trends in the Market

In this section we cover some of the low-field MR solutions currently available commercially and their main applications (see Table 1 for an overview of the systems and their specifications). Nearly all low-field scanners currently on the market are equipped with a permanent magnet made of neodymium-iron-boron, as discussed earlier. Such a magnet configuration has as its main advantages its low financial cost, no need for cooling systems, and low power consumption. In some cases, these MRI scanners only require a standard 220 V power supply. The most notable exceptions are scanners built around a resistive magnet and those with a high-temperature superconductive magnet made out of MgB₂. The average footprint of a whole-body low-field MR scanner ranges between 20 and 30 m², but the footprint of extremity scanners can be as small as 9 m² with the 5 Gauss line within their magnet cover. This makes the placement of these machines very versatile.

Most of the low-field scanners have an open design, replacing the standard cylindrical shape with two toroidal

magnets. The main applications for these scanners are scanning patients with claustrophobia more comfortably, the ability to scan obese patients, better patient positioning, and increased accessibility to the patients while scanning. Magnet bore openings vary widely, ranging from 35.1 cm up to 58 cm.

Integrating therapy and imaging is a growing technology over the last few years. Several low-field MR scanners that enable integrated radiotherapy using either Cobalt-60 sources or linear accelerators for irradiation are on the market or under development.^{41–46} These scanners have been developed in order to image the anatomy of a patient while performing radiation therapy, enabling better control of radiation dose. All of these systems cover the whole body and have gradient slew rates compared to other whole-body low-field MR systems (see Table 1).

Another clinical application that arises from using an open design is to image patients in body positions other than supine. Several low-field MRI scanners are specifically marketed for

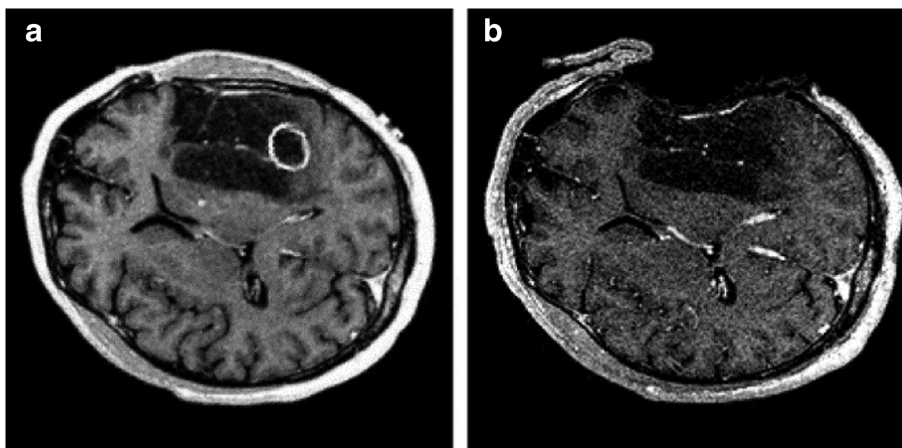


FIGURE 8: (a) Preoperative and (b) intraoperative MR scan (0.2T); speech-relevant areas are denoted in the preoperative data with a white circle. Significant brain shift has occurred, explaining the need for interoperative imaging for target assessment. Adapted from Hastreiter et al.⁴⁰

imaging patients in an upright, weight-bearing position. The main focus of these machines is musculoskeletal imaging, increasing, for example, the diagnostic accuracy in cartilage defects and osteoarthritis. An example of a case in which weight-bearing scans give more information can be seen in Fig. 7, in which the amount of vertebral disc protrusion becomes more evident in an upright position. However, many more topics of clinical relevance benefit from upright imaging; for example, vaginal prolapse and venous blood flow.^{43,44} Weight-bearing scans can be achieved by having a machine in which the magnets are aligned vertically, generating a “vertical bore” in which the patient can be upright or placed on a table.⁴⁵ Another solution is to build a rotatable magnet, which means that the patient can be scanned lying down or standing up.⁴⁶

One of the clinical applications related to the increased accessibility of low-field scanners is to guide interventions while the subject is within the scanner. In addition, the lower magnetic field usually results in lower fringe fields and less acoustic noise, both advantageous while performing an intervention. One example of a design that enables interventions is the OR-360° (MRI Operating Room, FONAR), which is a full-size room with a standard eight-foot ceiling. The two magnetic poles of the magnet are located in the center of the room. One of them protrudes from the ceiling and the other from the floor, leaving a large gap in which the patient lies and can be accessed from any angle. Some low-field scanners are made to be moveable, giving the medical staff the option to position the scanner around the hospital bed and remove it when it is no longer necessary. Several scanners specifically designed for interventional purposes have been brought to the market, eg, scanners that consist of two vertically oriented superconducting cylindrical magnets with operating space between them, and smaller systems that only surround the head of the patient that are designed for imaging during cranial surgery. Both options deliver the possibility to image while performing a surgical procedure,^{36–39} something that can be crucial when the anatomy is subject to large movements such as, for example, the brain shift that happens when the skull is opened, as shown in Fig. 8, adapted from Ref. 40. That being said, currently no vendor has a low-field MRI scanner specifically aimed at interventions in their catalog.

Finally, the smaller costs associated with a low-field MR scanner make it possible to have a valid business model even when the scanner is tailored to a specific body part such as the extremities (hand/wrist) rather than for the whole body. Due to their small size, such extremity scanners can achieve very high gradient strengths of up to 215 mT/m. This type of scanner can be placed closer to the patient in regional practices or hospitals, extending the diagnostic advantages of MRI. Similar designs with a very small footprint exist for imaging image neonates. Because the scanner has a single specific application, it can be tailor-made: in the case of a neonatal scanner this entails minimizing gradient noise and

including special features such as temperature control into the bed. Combined with the fact that it only requires 220 V and no cryogenics means that such a system can be placed within the neonatal ICU, which is an additional advantage.

New Acquisition Strategies

While the MRI contrast mechanisms and methods to exploit them have remained largely unchanged over the last decades, there have been some clear improvements in the implementation of readout strategies and image reconstruction that, combined with the longer T_2 relaxation times at low fields, can increase the SNR compared with the relatively simple acquisition and processing strategies used in earlier low-field applications.

The concept of echo planar readouts can be traced to the very start of MRI, and indeed echo volume imaging was proposed in the late 1970s and implemented in the late 1980s.⁴⁷ Gradient performance improvements together with the advent of parallel imaging with controlled aliasing^{48,49} made gradient echo encoding acquisitions viable. Even more advanced readout waveforms such as Wave-CAIPI^{50,51} or blipped stack of spirals⁵² are viable in systems with a large B_0 field homogeneity, but require gradients with fast slew rates.

3D-EPI methodologies have been successfully used to obtain high spatial resolution structural imaging at high fields with T_2^* weighting.^{53,54} Noting that T_2^* values are longer at lower field strengths (see Fig. 1), and that the resolution sought will be reduced (Eq. 2), single/few shot acquisitions can be envisaged as well as short-enough readouts for multiecho acquisition. In the case discussed earlier, ie, moving from 1.5 to 0.5T, the total echo train length could be reduced by a factor of 3 (resulting from $\frac{B_{0,L} \text{ power}_{\text{eff},w}}{B_{0,H}}$ accounting for the reduction of the readout length. Such an echo train, due to the longer T_2^* values (~ 1.5 times higher) can be, at 0.5T, accommodated in $\sim 22\%$ of the number of segments. The number calculated previously assumes the echo spacing between successive readouts remain unchanged, yet if the reduction in resolution is also considered in the readout direction (assuming gradient specifications remain similar to the equivalent high-field system acquisition), this can be further reduced. While it sounds counterintuitive to aim at faster imaging in the context of the lower SNR available at lower fields, it should be noted that magnitude image averaging after coregistration is less prone to image artifacts arising from subject displacement or other system drifts than k -space averaging (eg, acquiring separate segments or phase encoding steps). Such approaches have been used in the past to obtain ultrahigh-resolution (<0.5 mm) images at high field.⁵⁵

The same argument (ie, the possibility of acquiring longer echo trains) could be used for rapid acquisition with refocused echoes (RARE) and gradient- and spin-echo (GRASE) readouts,^{56–59} potentially combined with more advanced

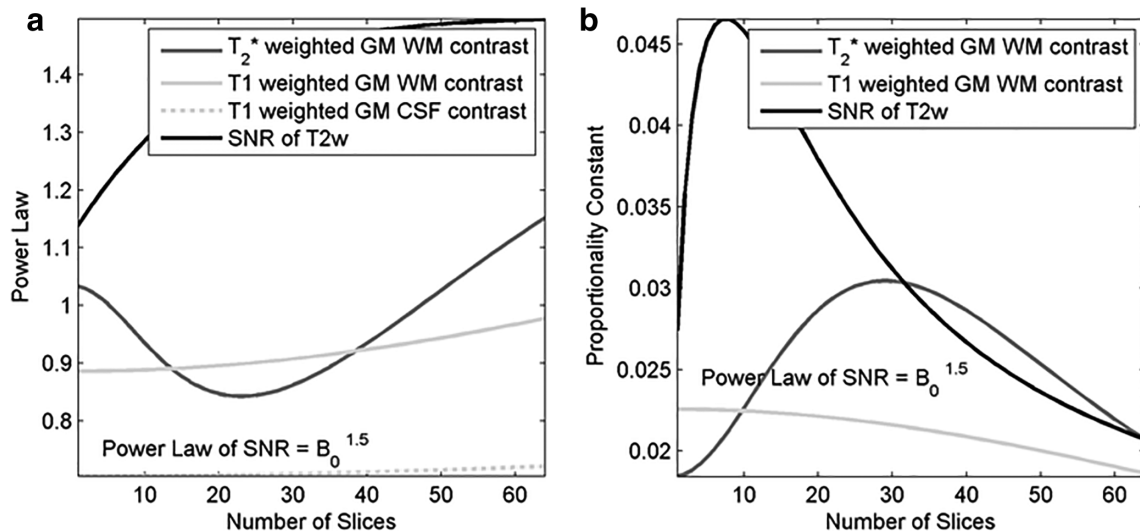


FIGURE 9: Plots of the (a) power law, $power_{eff,w}$ and (b) proportionality constant, c , dependence of SNR efficiency of different contrasts on the number of slices excited per TR when parameterizing it as $c B_0^{power_{eff,w}}$.

k -space trajectories.⁶⁰ In the case of refocusing pulses lower than 180 degrees (as used in variable flip angle refocusing trains), the effective signal decay rate is a function of both T_2 and T_1 . Therefore, the advantages of the longer T_2 s of tissues are counteracted by the shorter T_1 values that result in the attenuation of the signal throughout the echo train when long echo trains (greater than T_2) are used in 3D variants. In the context of refocused echo trains, another advantage at low fields is the possibility of using shorter RF pulses (as no SAR limitations are to be expected), as well as a more homogeneous contrast due to the increased B_1 homogeneity.⁶¹

The concept of simultaneous multislice (SMS) imaging was introduced in the early 1990s⁶² and rediscovered in combination with parallel imaging 10 years later.^{63,64} Recently, it has found widespread applications, particularly in the context of fMRI and diffusion imaging,⁶⁵ but also in structural imaging.^{60,66,67} Although SMS has been mainly developed and explored at high fields, it is a technique that would be straightforward to apply at lower fields and would find larger benefits there. At high fields the RF pulses used often sacrifice their bandwidth time product, their slice profile, or their length⁶⁸ because of SAR constraints ($SAR \propto B_0^2$). With SMS excitation, the number of excitation pulses needed to cover the whole volume is reduced by the SMS factor, allowing shorter repetition times for 2D sequences. Using the same assumption as earlier when evaluating the effective power law dependence of T_2^* - and T_1 -weighted imaging, the simulations outlined earlier in this article were repeated, now with the TR accommodating the number of separate excitations needed to cover the whole volume (see Fig. 9). It is interesting to note that in this regime the T_1 -contrast is reduced as the number of stacks to be excited increases, suggesting that high SMS factors are beneficial. However, for T_2^* -weighted contrast a maximum CNR is achieved when 20–30 excitations

are interleaved per TR, corresponding to an SMS factor of 3 to encode 60–90 slices over the volume. Other than functional imaging, SMS is used in T_2 -weighted and diffusion-weighted imaging. In such applications it offers the possibility to reduce the TR of the acquisitions to close to the optimum TR ($\sim 1.2 \times T_1$) when the magnetization is fully saturated upon excitation, as is the case when refocusing pulses are present in the readout process. At low field, because of the shorter T_1 of tissues, a relatively small number of slices is sufficient to make imaging in the regime inefficient and SMS excitation and refocusing would be particularly beneficial. Note that using high SMS factors does not have to come at the cost of high parallel imaging factors, and that a full encoding of k -space can be as effectively performed as in 3D imaging.⁵² As a consequence, high SMS factors do not require a high number of receiver coils per se.

At higher fields, it has been shown that performing motion tracking is critical to maximizing the SNR and sharpness of MR images.^{69,70} The relevance of motion tracking is greater when the spatial resolution of the image is higher. Following the discussion on SNR, it is clear that this is most relevant in the scenario described in Eq. 1, where the acquisition time at lower field strengths has to be increased to maintain the resolution achieved at higher field strengths. There have been various methods presented in the literature to perform either prospective or retrospective motion correction based on the use of external devices, or imaging or k -space navigators.⁶⁹ The complexity (and costs) associated with the integration and calibration of various devices suggests that using imaging navigators is a preferable avenue in the context of inexpensive imaging. Imaging navigators can be successfully used either prospectively or retrospectively, although they are mostly applicable to volumetric image acquisitions because of spin history effects.⁷¹ It is generally

accepted that the precision of motion parameters extracted from imaging navigators can be up to $1/10^{\text{th}}$ of their resolution, while the motions that need to be corrected to achieve visible improvements should be closer to $1/2$ of a voxel. In the context of low-field imaging, with long T_2 s and short T_1 values, an ideal approach would be the use of volume navigators, so-called vnavs.⁷² In this approach, the host sequence is interleaved with low flip angle (2°) low resolution (8 mm) 3D-EPI acquisition. Such navigators have been demonstrated to be able to correct 1 mm isotropic acquisitions at 3T. The lower resolutions needed at low field would suggest that this could be achieved with single-shot 3D EPVI acquisitions.

Most low-field systems, as reviewed earlier, are equipped with a relatively small number of receive channels. Other than economic motivations, parallel imaging is expected to be more prone to g-factor noise amplification due to the longer RF wavelength at lower field. Furthermore, parallel imaging is mostly used when there is already sufficient SNR, which can be traded by shortening the length of the acquisition. At 3T, it has been shown that for brain applications, acceleration factors of 9 or 13 can be achieved using 32-channel coils while keeping the maximum noise amplification under 10% and 35%, respectively, when using 3D controlled aliasing.^{50,60} It is conceivable that, at lower field with the typical 4–8 channels available, acceleration factors of 3 to 5 can be achieved. Alternatively, or increasingly commonly in combination with parallel imaging, compressed sensing can be used to accelerate the acquisition of images.² As discussed in the accelerated readouts section, these techniques can be used to reduce the motion sensitivity. In simulations, it has been demonstrated that such techniques can be used, even at low field, to image upper airway displacement in real time.⁷³

Future Avenues

In this article we reviewed some of the current trends in imaging with low-field MR scanners that use standard linear gradient encoding for image formation, and standard transmit and receive methods. We have not considered more experimental arrangements such as, for example, a gradient-less MR system,⁷⁴ using ultralow-field measurements combined with squid detection,^{75–77} use of Overhauser-enhanced MRI,⁷⁸ or fast field cycling approaches.⁷⁹ Another avenue that has not been discussed here, but which has potential in low-field scanners, is the use of specialized contrast agents,^{80,81} which, due to the field-dependent relaxometry parameters, can show increased T_1 enhancement at lower fields.⁸²

Currently, the major applications of low-field MRI in developed countries are in specialized applications, for example: 1) combining MRI with radiotherapy treatment and intervention, 2) allowing the patient to be imaged in either a horizontal or vertical position, or 3) imaging the extremities such as hand/wrist in a very small site.

One question that naturally arises is why should low-field MRI now be any more clinically relevant than low-field MRI several decades ago? Despite the advances in magnet, RF, and gradient technology, as well as imaging sequences outlined in this article, one is still constrained in terms of SNR by the lower Boltzmann distribution and induced voltage corresponding to the lower field strength. One reason we believe that low-field MRI can make great strides in terms of clinical relevance is the tremendous ongoing advances in image reconstruction, which not only allows diagnostically useful information to be obtained from much lower SNR images than previously, but also enable image reconstruction from data acquired with significant nonlinearities in magnetic field homogeneity and gradient linearity.

Currently, there is enormous interest in the use of machine-learning/artificial intelligence within the MRI community. From a low-field MRI point of view, one of the most promising aspects is its superior immunity to noise and a reduction in reconstruction artifacts compared with conventional reconstruction methods.^{4,5} Such reconstruction methods are also able to deal with a larger degree of gradient nonlinearity and magnet inhomogeneity, which are both hallmarks of low-field systems, and may indeed allow even less expensive systems than currently available to be designed. Provided the system is well characterized, gradient and magnet nonlinearities can be included directly in the reconstruction process.⁸³ The ability to obtain distortion-free images even in the presence of non/less-linear gradients could allow the use of, for example, monopolar gradients⁸⁴ that are suitable for some of the magnet designs used in low-field and portable MRI.

There are various other new developments in image acquisition and reconstruction that could be useful at lower field. One common critique of MRI in general is the large amount of possible image contrasts that imply a high level of specialization for the interpretation of these images (one of the cost drivers in MRI). It has been suggested that one means to overcome this is by embracing relaxometry and quantitative imaging, with MR fingerprinting potentially being an efficient technique to acquire such datasets,³ whose diagnostic value is now being evaluated.⁸⁵ MR fingerprinting typically uses a sequence of steady-state free-precession acquisitions where the flip angle or repetition times as well as the k-space sampling pattern are varied in a pseudorandom fashion to ensure that relaxation parameters within a given range can be robustly mapped. A dictionary is then used to estimate alias-free parameter maps. From an SNR efficiency point of view, the approximately linear dependence on the field strength found for T_1 -weighted and T_2^* -weighted imaging should also be found for MR fingerprinting. On the other hand, the longer readouts achievable (both due to the longer T_2 and reduced subject induced B_0 inhomogeneity in Hz) and reduced spatial resolution desired at lower fields will reduce the degree of undersampling of each individual image.

Thus, the signal dictionaries used to estimate relaxation parameters can be more efficiently used for parameter-estimation rather than artifact removal. Furthermore, the size of the dictionaries used can be significantly reduced thanks to the increased B_0 and B_1 homogeneity expected at lower field.

In terms of using compressed sensing, one issue is that when high acceleration factors are used the reconstructed images tend to show clear features associated with the type of regularization used (smooth, piecewise smooth, low rank are some examples of regularizations used). However, at low field, with the possibility of acquiring long readouts (and reduced resolution desired), such extreme accelerations might not be necessary. Furthermore, because there is an inherent need to increase the number of averages used to improve the SNR, it is conceivable to have the undersampling patterns of these independent measurements varied, as is performed in time resolved or dynamic imaging.^{86,87} The use of temporal constraints in addition to spatial constraints results in further reductions of regularization artifacts, while allowing separate estimations of object deformations and subject movement.

Many of the techniques brought up in this discussion are not yet fully deployed on today's high-field systems and a large fraction of clinical protocols in clinics for historical reasons does not use to the full extent current scanner capabilities. It is conceivable that in some cases low-field scanners could already provide sufficient information for diagnostic information, and that the slow integration of these new technologies at high field will trickle down to low-field scanners, making them more performant.

Acknowledgments

The authors thank Dr. Mike Poole (Hyperfine-research), Wim van den Broek (Radboud UMC, Nijmegen) and Prof. David G. Norris (Radboud University, Nijmegen) for the interesting discussions on the topic of this review article and the ERC Advanced Grant NOMA-MRI for supporting the research of A.W.

Conflicts of Interest

The authors have no conflicts of interests to declare.

References

- Magnetic Resonance Imaging (MRI) Systems Market worth 7.09 Billion USD by 2023. <https://www.marketsandmarkets.com/PressReleases/MRI-market.asp>. Accessed September 14, 2018.
- Lustig M, Donoho D, Pauly JM. Sparse MRI: The application of compressed sensing for rapid MR imaging. *Magn Reson Med* 2007;58:1182–1195.
- Ma D, Gulani V, Seiberlich N, et al. Magnetic resonance fingerprinting. *Nature* 2013;495:187–192.
- Hyun CM, Kim HP, Lee SM, Lee S, Seo JK. Deep learning for under-sampled MRI reconstruction. *Phys. Med. Biol.* 2018;63:135007.
- Zhu B, Liu JZ, Cauley SF, Rosen BR, Rosen MS. Image reconstruction by domain-transform manifold learning. *Nature* 2018;555:487–492.
- Health equipment — Magnetic resonance imaging (MRI) units — OECD Data. The OECD. <http://data.oecd.org/healtheqt/magnetic-resonance-imaging-mri-units.htm>. Accessed July 12, 2018.
- WHO | Atlas: Multiple Sclerosis Resources in the World 2008. WHO. http://www.who.int/mental_health/neurology/atlas_multiple_sclerosis_resources_2008/en/. Accessed July 12, 2018.
- Hayashi N, Watanabe Y, Masumoto T, et al. Utilization of low-field MR scanners. *Magn Reson Med Sci* 2004;3:27–38.
- Warf BC. Pediatric hydrocephalus in East Africa: Prevalence, causes, treatments, and strategies for the future. *World Neurosurg.* 2010;73:296–300.
- Macovski A. Noise in MRI. *Magn Reson Med* 1996;36:494–497.
- Rooney WD, Johnson G, Li X, et al. Magnetic field and tissue dependencies of human brain longitudinal (H₂O)-H-1 relaxation in vivo. *Magn Reson Med* 2007;57:308–318.
- Bottomley PA, Foster TH, Argersinger RE, Pfeifer LM. A review of normal tissue hydrogen NMR relaxation times and relaxation mechanisms from 1–100 MHz: Dependence on tissue type, NMR frequency, temperature, species, excision, and age. *Med Phys* 1998;11:425–448.
- Peters AM, Brookes MJ, Hoogenraad FG, et al. T2* measurements in human brain at 1.5, 3 and 7 T. *Magn Reson Imaging* 2007;25:748–753.
- Pohmann R, Speck O, Scheffler K. Signal-to-noise ratio and MR tissue parameters in human brain imaging at 3, 7, and 9.4 Tesla using current receive coil arrays. *Magn Reson Med* 2016;75:801–809.
- Jack CR, Bernstein MA, Fox NC, et al. The Alzheimer's Disease Neuroimaging Initiative (ADNI): MRI methods. *J Magn Reson Imaging JMRI* 2008;27:685–691.
- Simon HE. A whole-body nuclear magnetic-resonance (NMR) imaging-system with full 3-dimensional capabilities. *Proc Soc Photo-Opt Instrum Eng* 1981;273:41–49.
- Warner R, Pittard S. Magnets. In: *Magnetic resonance technology*. 2016. pp. 48–80.
- Chen J, Wang D, Cheng S, et al. A hysteresis model based on linear curves for NdFeB permanent magnet considering temperature effects. *IEEE Trans Magn* 2018;54:1–5.
- Miyake T, Akai H. Quantum theory of rare-earth magnets. *J Phys Soc Jpn* 2018;87:041009.
- Nasu S, Hinomura T, Hirotsawa S, Kanekiyo H. Magnetic properties of Nd-Fe-B nanocrystalline composite. *Phys B Condens Matter* 1997;237–238:283–285.
- Tadic F, Tallone BG. Design and optimization of a novel bored biplanar permanent-magnet assembly for hybrid magnetic resonance imaging systems. *IEEE Trans Magn* 2010;46:4052–4058.
- Zhang Y, Xie D, Bai B, Yoon HS, Koh CS. A novel optimal design method of passive shimming for permanent MRI Magnet. *IEEE Trans Magn* 2008;44:1058–1061.
- Lopez HS, Liu F, Weber E, Crozier S. Passive shim design and a shimming approach for biplanar permanent magnetic resonance imaging magnets. *IEEE Trans Magn* 2008;44:394–402.
- Terada Y, Kono S, Ishizawa K, et al. Magnetic field shimming of a permanent magnet using a combination of pieces of permanent magnets and a single-channel shim coil for skeletal age assessment of children. *J Magn Reson* 2013;230:125–133.
- McGinley JVM, Ristic M, Young IR. A permanent MRI magnet for magic angle imaging having its field parallel to the poles. *J Magn Reson San Diego CA* 1997 2016;271:60–67.
- Martens MA, Petropoulos LS, Brown RW, Andrews JH, Morich MA, Patrick JL. Insertable biplanar gradient coils for magnetic resonance imaging. *Rev Sci Instrum* 1991;62:2639–2645.
- Zhang R, Xu J, Fu Y, et al. An optimized target-field method for MRI transverse biplanar gradient coil design. *Meas Sci Technol* 2011;22:125505.

28. While PT, Forbes LK, Crozier S. 3D gradient coil design for open MRI systems. *J Magn Reson* 2010;207:124–133.
29. Matsuzawa K, Abe M, Kose K, Terada Y. Oval gradient coils for an open magnetic resonance imaging system with a vertical magnetic field. *J Magn Reson* 2017;278:51–59.
30. Pšibíl J, Pšibílová A, Frollo I. Vibration and noise in magnetic resonance imaging of the vocal tract: differences between whole-body and open-air devices. *Sensors* 2018;18.
31. Su S, Zou MX, Murphy-Boesch J. Solenoidal array coils. *Magn Reson Med* 2002;47:794–799.
32. Roemer PB, Edelstein WA, Hayes CE, Souza SP, Mueller OM. The NMR phased array. *Magn Reson Med* 1990;16:192–225.
33. Pruessmann KP, Weiger M, Scheidegger MB, Boesiger P. SENSE: sensitivity encoding for fast MRI. *Magn Reson Med* 1999;42:952–962.
34. Griswold MA, Jakob PM, Heidemann RM, et al. Generalized autocalibrating partially parallel acquisitions (GRAPPA). *Magn Reson Med* 2002;47:1202–1210.
35. Vojtišek L, Frollo I, Valkovič L, Gogola D, Juráš V. Phased array receiving coils for low field lungs MRI: Design and optimization. *Meas Sci Rev* 2011;11:61–66.
36. García S, Reyes L, Roldán P, et al. Does low-field intraoperative magnetic resonance improve the results of endoscopic pituitary surgery? Experience of the implementation of a new device in a referral center. *World Neurosurg.* 2017;102:102–110.
37. DiMaio SP, Pieper S, Chinzei K, et al. Robot-assisted needle placement in open MRI: system architecture, integration and validation. *Comput. Aided Surg* 2007;12:15–24.
38. Walker DG, Talos F, Bromfield EB, Black PM. Intraoperative magnetic resonance for the surgical treatment of lesions producing seizures. *J Clin Neurosci* 2002;9:515–520.
39. von Tempelhoff W, Toktamis S, Schwarzmeier H-J, Eickmeyer F, Niehoff H, Ulrich F. LITT (Laser Induced Interstitial Thermoablation) of benign and malignant gliomas in the OPEN MR (0.5 Tesla, GE Signa SP). *Med Laser Appl* 2002;17:170–178.
40. Hastreiter P, Rezk-Salama C, Soza G, et al. Strategies for brain shift evaluation. *Med Image Anal* 2004;8:447–464.
41. Yang Y, Cao M, Sheng K, et al. Longitudinal diffusion MRI for treatment response assessment: Preliminary experience using an MRI-guided tritacort 60 radiotherapy system. *Med Phys* 2016;43:1369–1373.
42. Wojcieszynski AP, Rosenberg SA, Brower JV, et al. Gadaxetate for direct tumor therapy and tracking with real-time MRI-guided stereotactic body radiation therapy of the liver. *Radiother Oncol J Eur Soc Ther Radiol Oncol* 2016;118:416–418.
43. Abdulaziz M, Stothers L, Macnab A. Methodology for 3D image reconstruction of the female pelvis from upright open MRI (MRO) 2D imaging. *Biomed Spectrosc Imaging* 2018;7:81–96.
44. Partsch H, Mosti G, Uhl J-F. Unexpected venous diameter reduction by compression stocking of deep, but not of superficial veins. *Veins Lymphat* 2012;1:3.
45. Tarantino U, Fanucci E, Iundusi R, et al. Lumbar spine MRI in upright position for diagnosing acute and chronic low back pain: statistical analysis of morphological changes. *J Orthop Traumatol* 2013;14:15–22.
46. Satragno L, Biglieri E, Rezzonico F, Pugliese O, Contrada O, Alessandro T. *Magnetic resonance imaging apparatus*. 2011. <https://patents.google.com/patent/US8064984/en>.
47. Mansfield P, Howseman AM, Ordidge RJ. Volumar imaging using NMR spin echoes: echo-volumar imaging (EVI) at 0.1 T. *J Phys [E]* 1989;22:324.
48. Breuer FA, Blaimer M, Mueller MF, et al. Controlled aliasing in volumetric parallel imaging (2D CAIPIRINHA). *Magn Reson Med* 2006;55:549–556.
49. Narsude M, Gallichan D, van der Zwaag W, Gruetter R, Marques JP. Three-dimensional echo planar imaging with controlled aliasing: A sequence for high temporal resolution functional MRI. *Magn Reson Med* 2016;75:2350–2361.
50. Bilgic B, Gagoski BA, Cauley SF, et al. Wave-CAIPI for highly accelerated 3D imaging. *Magn Reson Med* 2015;73:2152–2162.
51. Cauley SF, Setsompop K, Bilgic B, Bhat H, Gagoski B, Wald LL. Autocalibrated wave-CAIPI reconstruction; Joint optimization of k-space trajectory and parallel imaging reconstruction. *Magn Reson Med* 2017;78:1093–1099.
52. Zahneisen B, Poser BA, Ernst T, Stenger VA. Three-dimensional Fourier encoding of simultaneously excited slices: generalized acquisition and reconstruction framework. *Magn Reson Med* 2014;71:2071–2081.
53. Langkammer C, Bredies K, Poser BA, et al. Fast quantitative susceptibility mapping using 3D EPI and total generalized variation. *NeuroImage* 2015;111:622–630.
54. Sati P, Thomasson DM, Li N, et al. Rapid, high-resolution, whole-brain, susceptibility-based MRI of multiple sclerosis. *Mult Scler* 2014;20:1464–1470.
55. Federau C, Gallichan D. Motion-correction enabled ultra-high resolution in-vivo 7T-MRI of the brain. *PLoS One* 2016;11:e0154974.
56. Alsop DC. The sensitivity of low flip angle RARE imaging. *Magn Reson Med* 1997;37:176–184.
57. Hennig J. RARE imaging: A fast imaging method for clinical MR. *J Magn Reson* 1988;78:397–407.
58. Oshio K, Feinberg DA. GRASE (gradient- and spin-echo) imaging: a novel fast MRI technique. *Magn Reson Med* 1991;20:344–349.
59. Mugler JP. Improved three-dimensional GRASE imaging with the SORT phase-encoding strategy. *J Magn Reson Imaging* 1999;9:604–612.
60. Gagoski BA, Bilgic B, Eichner C, et al. RARE/turbo spin echo imaging with simultaneous multislice Wave-CAIPI. *Magn Reson Med* 2015;73:929–938.
61. Zwanenburg JJM, Hendrikse J, Visser F, Takahara T, Luijten PR. Fluid attenuated inversion recovery (FLAIR) MRI at 7.0 Tesla: comparison with 1.5 and 3.0 Tesla. *Eur Radiol* 2010;20:915–922.
62. Glover GH. Phase-offset multiplanar (POMP) volume imaging: a new technique. *J Magn Reson Imaging JMRI* 1991;1:457–461.
63. Larkman DJ, Hajnal JV, Herlihy AH, Coutts GA, Young IR, Ehnholm G. Use of multicoil arrays for separation of signal from multiple slices simultaneously excited. *J Magn Reson Imaging* 2001;13:313–317.
64. Breuer FA, Blaimer M, Heidemann RM, Mueller MF, Griswold MA, Jakob PM. Controlled aliasing in parallel imaging results in higher acceleration (CAIPIRINHA) for multi-slice imaging. *Magn Reson Med* 2005;53:684–691.
65. Ugurbil K, Xu J, Auerbach EJ, et al. Pushing spatial and temporal resolution for functional and diffusion MRI in the Human Connectome Project. *Neuroimage* 2013;80:80–104.
66. Schulz J, P Marques J, Ter Telgte A, et al. Clinical application of Half Fourier Acquisition Single Shot Turbo Spin Echo (HASTE) imaging accelerated by simultaneous multi-slice acquisition. *Eur J Radiol* 2018;98:200–206.
67. Schulz J, Boyacıoğlu R, Norris DG. Multiband multislab 3D time-of-flight magnetic resonance angiography for reduced acquisition time and improved sensitivity. *Magn Reson Med* 2016;75:1662–1668.
68. Barth M, Breuer F, Koopmans PJ, Norris DG, Poser BA. Simultaneous multislice (SMS) imaging techniques. *Magn Reson Med* 2016;75:63–81.
69. Maclaren J, Herbst M, Speck O, Zaitsev M. Prospective motion correction in brain imaging: a review. *Magn Reson Med* 2013;69:621–636.
70. Maclaren J, Armstrong BSR, Barrows RT, et al. Measurement and correction of microscopic head motion during magnetic resonance imaging of the brain. *PLoS One* 2012;7:e48088.
71. Gallichan D, Marques JP. Optimizing the acceleration and resolution of three-dimensional fat image navigators for high-resolution motion correction at 7T. *Magn Reson Med* 2016;547–558.

72. Tisdall MD, Hess AT, Reuter M, Meintjes EM, Fischl B, van der Kouwe AJW. Volumetric navigators for prospective motion correction and selective reacquisition in neuroanatomical MRI. *Magn Reson Med* 2012;68:389–399.
73. Wu Z, Chen W, Nayak KS. Minimum field strength simulator for proton density weighted MRI. *PLoS One* 2016;11.
74. Cooley CZ, Stockmann JP, Armstrong BD, et al. Two-dimensional imaging in a lightweight portable MRI scanner without gradient coils. *Magn Reson Med* 73:872–883.
75. Espy M, Matlashov A, Volegov P. SQUID-detected ultra-low field MRI. *J Magn Reson* 2013;229:127–141.
76. Espy MA, Magnelind PE, Matlashov AN, et al. Progress toward a deployable SQUID-based ultra-low field MRI system for anatomical imaging. *IEEE Trans Appl Supercond* 2015;25:1–5.
77. Vesanen PT, Nieminen JO, Zevenhoven KCJ, et al. Hybrid ultra-low-field MRI and magnetoencephalography system based on a commercial whole-head neuromagnetometer. *Magn Reson Med* 2013;69:1795–1804.
78. Waddington DEJ, Sarracanie M, Salameh N, Herisson F, Ayata C, Rosen MS. An Overhauser-enhanced-MRI platform for dynamic free radical imaging in vivo. *NMR Biomed* 2018;31:e3896.
79. Ross PJ, Broche LM, Lurie DJ. Rapid field-cycling MRI using fast spin-echo. *Magn Reson Med* 2015;73:1120–1124.
80. Geninatti-Crich S, Szabo I, Alberti D, Longo D, Aime S. MRI of cells and mice at 1 and 7 Tesla with Gd-targeting agents: when the low field is better! *Contrast Media Mol Imaging* 2011;6:421–425.
81. Yin X, Russek SE, Zabow G, et al. Large T1 contrast enhancement using superparamagnetic nanoparticles in ultra-low field MRI. *Sci Rep* 2018;8.
82. Rohrer M, Bauer H, Mintorovitch J, Requardt M, Weinmann H-J. Comparison of magnetic properties of MRI contrast media solutions at different magnetic field strengths. *Invest Radiol* 2005;40:715–724.
83. Galiana G, Stockmann Jp, Tam L, Peters D, Tagare H, Constable RT. The role of nonlinear gradients in parallel imaging: A k-space based analysis. *Concepts Magn Reson Part Bridg Educ Res* 2012;40A:253–267.
84. Littin S, Gallichan D, Welz AM, et al. Monoplanar gradient system for imaging with nonlinear gradients. *Magn Reson Mater Phys Biol Med* 2015;28:447–457.
85. Panda A, Mehta BB, Coppo S, et al. Magnetic resonance fingerprinting — An overview. *Curr Opin Biomed Eng* 2017;3:56–66.
86. Otazo R, Candès E, Sodickson DK. Low-rank and sparse matrix decomposition for accelerated dynamic MRI with separation of background and dynamic components. *Magn Reson Med* 2015;73:1125–1136.
87. Piccini D, Feng L, Bonanno G, et al. Four-dimensional respiratory motion-resolved whole heart coronary MR angiography. *Magn Reson Med* 2017;77:1473–1484.